Lecture 7: The Swift-Hohenberg equation in one spatial dimension

Edgar Knobloch: notes by Vamsi Krishna Chalamalla and Alban Sauret
with substantial editing by Edgar Knobloch

January 10, 2013

1 Introduction

Let us consider the Swift-Hohenberg equation in one spatial dimension:

$$u_t = r\,u - (q_c^2 + \partial_x^2)^2\,u + f(u). \tag{1}$$

Here $f(u)$ represents the nonlinear terms in u and r is the bifurcation parameter. The parameter q_c represents a characteristic wavenumber, i.e., it selects a characteristic lengthscale given by $2\pi/q_c$. In unbounded domains the wavenumber q_c can be set equal to $q_c = 1$ but this is not the case on finite domains.

Despite its simplicity, Eq. (1) has very remarkable properties and we shall use it here as a "normal form" for systems exhibiting spatially localized structures on the real line. The equation is of fourth order in x and reversible in space, i.e., it is equivariant under $x \to -x$, $u \to u$. Motivated by the experiments summarized in the previous lecture we select a *bistable* nonlinearity of the form $f(u) = b_2u^2 - u^3$ (hereafter SH23) and $f(u) = b_3u^3 - u^5$ (hereafter SH35), with $b_2 > 0$ (resp., $b_3 > 0$); the latter nonlinearity leads to an additional symmetry, $x \to x$, $u \to -u$, that plays an important role in the properties of the solutions and is analogous to the so-called Boussinesq symmetry of Rayleigh-Bénard convection with identical boundary conditions at the top and bottom.

Equation (1) has variational structure, i.e., it possesses a Lyapunov functional $F[u(x,t)]$, such that

$$u_t = -\frac{\delta F}{\delta u}, \tag{2}$$

where F is given by

$$F = \int_{-\infty}^{\infty} \mathrm{d}x \left[-\frac{1}{2}\,r\,u^2 + \frac{1}{2}\left[(q_c^2 + \partial_x^2)\,u\right]^2 - \int_0^u f(v)\,\mathrm{d}v \right]. \tag{3}$$

It follows that

$$\frac{\mathrm{d}F}{\mathrm{d}t} = -\left(\frac{\partial u}{\partial t}\right)^2 \le 0, \tag{4}$$

and hence that $\mathrm{d}F/\mathrm{d}t < 0$ provided $\partial u/\partial t \neq 0$ somewhere in the domain. Thus on a finite domain with null boundary conditions all solutions evolve towards stationary states; on an

unbounded or periodic domain solutions in the form of moving fronts are possible. In the following we will think of the functional $F[u]$ as the (free) energy of the system. Stable (unstable) solutions correspond to local minima (maxima) of this energy. We shall see that in appropriate parameter regimes the energy landscape described by the free energy (3) can be exceedingly complex.

2 Linear stability of the uniform state

2.1 The temporal view

The usual way to examine the stability of the state $u = 0$ is to linearize Eq. (1) about this state and look for solutions of the form $u \propto \exp(\sigma_k t + ikx)$, where σ_k is the growth rate of a perturbation with wavenumber k. The growth rate σ_k is given by the dispersion relation

$$\sigma_k = r - (q_c^2 - k^2)^2. \tag{5}$$

The marginal stability curve is determined by setting $\sigma_k = 0$ and then minimizing the marginal value $r = r_k$ with respect to the wavenumber k. This calculation leads to the prediction $r = 0$ for the onset of instability, and of the associated wavenumber, $k = q_c$.

Observe that if one takes $r < 0$ then the condition for marginal stability, $r = (q_c^2 - k^2)^2$, has no solution for real k but it does have a solution with k complex. In contrast, if $r > 0$ there is a pair of real solutions, $k = k_\pm$, with $k_- < q_c < k_+$. As r decreases to zero from above the wavenumbers $k_\pm$ approach $k = q_c$ from opposite directions and at $r = 0$ they collide at $k = q_c$. Thus the minimum of the marginal stability curve is in fact associated with the collision of two roots of the marginal dispersion relation.

2.2 The spatial view

We can appreciate what is happening if we focus on steady states from the outset. These satisfy the ordinary differential equation (ODE)

$$r\,u - \left(q_c^2 + \frac{\mathrm{d}^2}{\mathrm{d}x^2}\right)^2 u + f(u) = 0. \tag{6}$$

As explained at the end of the preceding lecture we can also study the stability of the trivial flat state $u = 0$ *in space* by linearizing (6) around the $u = 0$ state and looking for solutions of the form $u \propto \exp(\lambda\, x)$. We obtain

$$(q_c^2 + \lambda^2)^2 - r = 0. \tag{7}$$

For $r < 0$ the spatial eigenvalues of $u = 0$ form a complex quartet (see Fig. 1a). At $r = 0$ these eigenvalues collide pairwise on the imaginary axis (see Fig. 1b) and for $r > 0$ they split but remain on the imaginary axis (see Fig. 1c) [3]. It should be evident that the temporal and spatial points of view are closely related; in particular, the onset of instability in the temporal point of view is equivalent to the presence of a pair of purely imaginary spatial eigenvalues of double multiplicity.

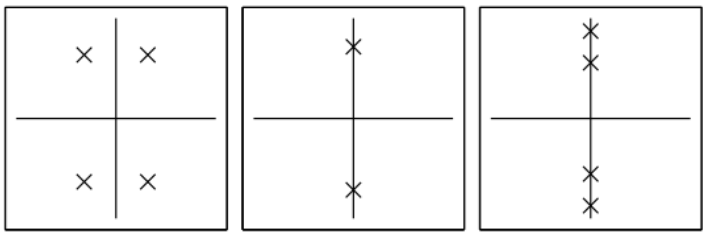

Figure 1: The behavior of the spatial eigenvalues λ of $u = 0$. (a) $r < 0$, (b) $r = 0$, (c) $r > 0$.

It is useful to look at the transition at $r = 0$ in a little more detail. We write $r = \epsilon^2\mu$, where $\mu = \mathcal{O}(1)$ and $\epsilon \ll 1$. We then find that for $\mu < 0$ the spatial eigenvalues are $\lambda = \pm\epsilon(2q_c)^{-1}\sqrt{-\mu} \pm i(q_c + \mathcal{O}(\epsilon^2))$ while for $\mu > 0$ the eigenvalues are $\lambda = \pm i\epsilon(2q_c)^{-1}\sqrt{\mu} \pm i(q_c + \mathcal{O}(\epsilon^2))$. These considerations suggest that when $r < 0$ the solutions near $u = 0$ will be growing or decaying as $u \sim \exp(\pm\epsilon\sqrt{-\mu}\, x/2q_c)$, i.e., that the amplitude of such solutions will vary on a long scale $X \equiv \epsilon x$ while their wavenumber will remain close to q_c. We will take advantage of this insight in the next section.

3 Weakly nonlinear analysis

We now consider the steady states of SH35 with $f(u) = b_3\, u^3 - b_5\, u^5$ (SH35); the coefficient b_5 can be scaled to unity but is retained here to emphasize the contribution of the fifth order term. The steady states satisfy the ODE

$$r\, u - \left(q_c^2 + \frac{\mathrm{d}^2}{\mathrm{d}x^2}\right)^2 u + b_3\, u^3 - b_5\, u^5 = 0. \tag{8}$$

Because of the symmetry $x \to x$, $u \to -u$ the weakly nonlinear theory for this case is simpler than for SH23. Indeed, we can establish the presence of homoclinic orbits near $r = 0$ by setting $r \equiv \epsilon^2\, \mu < 0$ with $\mu = \mathcal{O}(1)$. As suggested by the linear theory in the preceding section we use a multiple scale expansion with spatial scales x and $X \equiv \epsilon\, x$, and introduce the Ansatz:

$$u_\ell(x) = \epsilon\, u_1(x, X) + \epsilon^2\, u_2(x, X) + ..., \tag{9}$$

where

$$u_1(x, X) = Z(X; \epsilon)\, \mathrm{e}^{iq_c\, x} + c.c. \tag{10}$$

The following calculation determines $Z(X; \epsilon)$. For reasons that will become apparent the calculation needs to be done to fifth order in the small parameter ϵ. For this reason it is simplest to perform the calculation at $r = 0$ and then figure out what additional terms involving μ have to be added. We begin by writing

$$\frac{\mathrm{d}}{\mathrm{d}x} = \frac{\partial}{\partial x} + \epsilon\, \frac{\partial}{\partial X}. \tag{11}$$

Matching terms order by order in ϵ gives:

$$\begin{aligned}
\mathcal{O}(\epsilon) : (\partial_x^2 + q_c^2)^2\, u_1 &= 0 && (12)\\
\mathcal{O}(\epsilon^2) : (\partial_x^2 + q_c^2)^2\, u_2 &= -4\partial_{xX}\,(\partial_x^2 + q_c^2)\, u_1 && (13)\\
\mathcal{O}(\epsilon^3) : (\partial_x^2 + q_c^2)^2\, u_3 &= -4\partial_{xX}\,(\partial_x^2 + q_c^2)\, u_2 - 4\,\partial_{xxXX} u_1 - 2\partial_{XX}(\partial_x^2 + q_c^2) u_1 + b_3\, u_1^3 && (14)\\
\mathcal{O}(\epsilon^4) : (\partial_x^2 + q_c^2)^2\, u_4 &= -4\partial_{xX}\,(\partial_x^2 + q_c^2)\, u_3 - 4\,\partial_{xxXX} u_2 - 2\partial_{XX}(\partial_x^2 + q_c^2) u_2 \\
&\quad -4\,\partial_{xXXX} u_1 + 3\, b_3\, u_1^2\, u_2 && (15)\\
\mathcal{O}(\epsilon^5) : (\partial_x^2 + q_c^2)^2\, u_5 &= -4\partial_{xX}\,(\partial_x^2 + q_c^2)\, u_4 - 4\,\partial_{xxXX} u_3 - 2\partial_{XX}(\partial_x^2 + q_c^2) u_3 \\
&\quad -4\,\partial_{xXXX} u_2 - \partial_X^4\, u_1 + 3\, b_3\,(u_1\, u_2^2 + u_1^2\, u_3) - b_5\, u_1^5. && (16)
\end{aligned}$$

We solve these equations order by order. The $\mathcal{O}(\epsilon, \epsilon^2)$ equations are solved by

$$u_1(x, X) = A_1(X) \mathrm{e}^{i\, q_c\, x} + c.c., \qquad u_2(x, X) = A_2(X) \mathrm{e}^{i\, q_c\, x} + c.c., \tag{17}$$

where $A_{1,2}(X)$ are as yet undetermined and *c.c.* denotes a complex conjugate. The Ansatz

$$u_3(x, X) = A_3(X) \mathrm{e}^{i\, q_c\, x} + C_3(X) \mathrm{e}^{3\, i\, q_c\, x} + c.c. \tag{18}$$

in the $\mathcal{O}(\epsilon^3)$ equation leads to the two results

$$4\, q_c^2\, A_1'' = -3\, b_3\, A_1\, |A_1|^2, \qquad C_3 = \frac{b_3}{64\, q_c^4}\, A_1^3, \tag{19}$$

with A_3 arbitrary. The Ansatz

$$u_4(x, X) = A_4(X) \mathrm{e}^{i\, q_c\, x} + C_4(X) \mathrm{e}^{3\, i\, q_c\, x} + c.c. \tag{20}$$

in the $\mathcal{O}(\epsilon^4)$ equation likewise leads to

$$4\, q_c^2\, A_2'' = 4\, i q_c\, A_1''' - 3\, b_3\, (2\, |A_1|^2\, A_2 + A_1^2\, \bar{A}_2); \tag{21}$$

the expression for C_4 in terms of $A_{1,2}$ is not needed in what follows. Finally, the $\mathcal{O}(\epsilon^5)$ equation with the Ansatz

$$u_5(x, X) = A_5(X) \mathrm{e}^{i\, q_c\, x} + C_5(X) \mathrm{e}^{3\, i\, q_c\, x} + E_5(X) \mathrm{e}^{5\, i\, q_c\, x} + c.c. \tag{22}$$

yields

$$\begin{aligned}
4\, q_c^2\, A_3'' &= 4\, i\, q_c\, A_2''' + A_1'''' - 3\, b_3\, (2\, A_1\, |A_2|^2 + \bar{A}_1\, A_2^2 + 2\, |A_1|^2\, A_3 + A_1^2\, \bar{A}_3) \\
&\quad + \left(-\frac{3\, b_3^2}{64\, q_c^4} + 10\, b_5 \right) A_1\, |A_1|^4
\end{aligned} \tag{23}$$

after elimination of C_3. Equations (19), (21) and (23) can now be assembled into a single equation for $Z(X, \epsilon) \equiv A_1(X) + \epsilon\, A_2(X) + \epsilon^2\, A_3(X) + ...$,

$$4\, q_c^2\, Z'' = -3\, b_3 Z\, |Z|^2 + 4\, i\, q_c\, \epsilon\, Z''' + \epsilon^2 \left[Z'''' + \left(-\frac{3\, b_3^2}{64\, q_c^2} + 10\, b_5 \right) Z\, |Z|^4 \right] + \mathcal{O}(\epsilon^3). \tag{24}$$

The higher derivatives can be eliminated iteratively, resulting in the amplitude equation

$$4\,q_c^2\,Z'' = -3\,b_3 Z\,|Z|^2 - \frac{3\,i\,\epsilon\,b_3}{q_c}\left(2\,Z'|Z|^2 + Z^2\,\bar{Z}'\right) + \epsilon^2\left[\frac{9\,b_3}{2\,q_c^2}\left(2\,Z\,|Z'|^2 + (Z')^2\,\bar{Z}\right) + \left(-\frac{327\,b_3^2}{64\,q_c^4} + 10\,b_5\right) Z\,|Z|^4\right] + \mathcal{O}(\epsilon^3). \quad (25)$$

Equation (25) represents the Ginzburg-Landau approximation to the Swift-Hohenberg equation (8) at $r = 0$ [5].

4 Normal form theory

The linear problem at $r = 0$ is degenerate because the purely imaginary eigenvalues $\lambda = \pm i q_c$ have *double multiplicity*. The presence of this degeneracy is a consequence of the spatial reversibility of the equation and this fact allows us to make use of normal form theory developed for a Hopf bifurcation in systems that are reversible in time. For this reason the bifurcation at $r = 0$ is often referred to as the reversible Hopf bifurcation with $1:1$ resonance or sometimes as the Hamiltonian-Hopf bifurcation.[1] The normal form for this bifurcation is derived and analyzed in [9], and is given by

$$\dot{A} = i\,q_c\,A + B + i\,A\,P(\mu; y, w), \quad (26)$$
$$\dot{B} = i\,q_c\,B + i\,B\,P(\mu; y, w) + A\,Q(\mu; y, w), \quad (27)$$

where $y \equiv |A|^2$, $w \equiv \frac{i}{2}(A\,\bar{B} - \bar{A}\,B)$. Here μ is the bifurcation parameter and P and Q are (infinite) polynomials with real coefficients:

$$P(\mu; y, w) = p_1\,\mu + p_2\,y + p_3\,w + p_4\,y^2 + p_5\,w\,y + p_6\,w^2 + ..., \quad (28)$$
$$Q(\mu; y, w) = -q_1\,\mu + q_2\,y + q_3\,w + q_4\,y^2 + q_5\,w\,y + q_6\,w^2 + ... \quad (29)$$

Although these equations look quite different from the equation obtained through multiple scale analysis the two calculations are in fact one and the same. To see this we set $\mu = 0$ and write $(A, B) = (\epsilon\,\tilde{A}(X), \epsilon^2\,\tilde{B}(X))\mathrm{e}^{i\,q_c\,x}$, obtaining

$$\epsilon^2 A' = \epsilon^2 B + i\epsilon A\left[\epsilon^2 p_2\,|A|^2 + \epsilon^3 p_3\,\frac{i}{2}(A\,\bar{B} - \bar{A}B)\right] + \mathcal{O}(\epsilon^5), \quad (30)$$

$$\epsilon^3\,B' = i\,\epsilon^2\,B\left[\epsilon^2\,p_2\,|A|^2 + \epsilon^3\,p_3\,\frac{i}{2}\,(A\,\bar{B} - \bar{A}B)\right] + \epsilon\,A\left[\epsilon^2\,q_2\,|A|^2 + \epsilon^3\,q_3\,\frac{i}{2}\,(A\bar{B} - \bar{A}B) + \epsilon^4 q_4|A|^4\right] + \mathcal{O}(\epsilon^6). \quad (31)$$

Equation (30) now yields a power series expansion for B in terms of A,

$$B = A' - i\,\epsilon\,p_2\,A\,|A|^2 + \epsilon^2\,\frac{p_3}{2}\,A\,(A\bar{A}' - \bar{A}A') + \mathcal{O}(\epsilon^3), \quad (32)$$

[1] Hamiltonian systems are reversible in time; eq. (8) is in fact a Hamiltonian system in space [11]

and this equation can be used to eliminate B from Eq. (31):

$$\begin{aligned} A'' &= q_2\, A\,|A|^2 + i\,\epsilon\left[\left(3\,p_2 - \frac{1}{2}\,q_3\right) A'|A|^2 + \left(p_2 + \frac{1}{2}\,q_3\right) A^2\,\bar{A}'\right] \\ &\quad +\epsilon^2\left[p_3\,((A')^2\,\bar{A} - A\,A'\,\bar{A}') + (q_4 - q_3\,p_2 + p_2^2)\,A\,|A|^4\right] + \mathcal{O}(\epsilon^3). \end{aligned} \tag{33}$$

Finally, writing $Z = A + \epsilon^2\,\rho\,A\,|A|^2 + \mathcal{O}(\epsilon^4)$ allows one to compare the result with Eq. (25) and thereby deduce the normal coefficients:

$$\rho = \frac{9\,b_3}{16\,q_c^4}, \quad p_2 = -\frac{9\,b_3}{16\,q_c^3}, \quad q_2 = -\frac{3\,b_3}{4\,q_c^2}, \quad p_3 = 0, \quad q_3 = -\frac{3\,b_3}{8\,q_c^3}, \quad q_4 = -\frac{177\,b_3^2}{128\,q_c^6} + \frac{5\,b_5}{2\,q_c^2}. \tag{34}$$

The remaining coefficients p_1 and q_1 are determined as part of the *unfolding*. This term is used to refer to the reintroduction of the bifurcation parameter into the description. As indicated earlier, we write $r = \epsilon^2\,\mu < 0$, where $\mu = \mathcal{O}(1)$, and compute the resulting linear terms. The unfolded version of (33) through $\mathcal{O}(\epsilon)$ is

$$\begin{aligned} A'' &= -q_1\,\mu\,A + q_2\,A\,|A|^2 + i\,\epsilon\Bigg[2\,p_1\,\mu\,A' + \left(3\,p_2 - \frac{1}{2}\,q_3\right) A'\,|A|^2 \\ &\quad + \left(p_2 + \frac{1}{2}\,q_3\right) A^2\,\bar{A}'\Bigg] + \mathcal{O}(\epsilon^2) \end{aligned} \tag{35}$$

and since $Z = A + \mathcal{O}(|A|^2 A)$ this equation corresponds to the amplitude equation [5]

$$4\,q_c^2\,Z'' = -\mu\,Z - 3\,b_3\,Z\,|Z|^2 + \frac{i\,\epsilon}{q_c}\left[-\mu\,Z' - 3\,b_3\,(2\,Z'\,|Z|^2 + Z^2\bar{Z}')\right] + \mathcal{O}(\epsilon^2). \tag{36}$$

Matching terms through linear order gives

$$p_1 = -\frac{1}{8\,q_c^3}, \qquad q_1 = \frac{1}{4\,q_c^2}. \tag{37}$$

5 Homoclinics and heteroclinics

The normal form (26)–(27) is completely integrable [9], with integrals

$$K \equiv \frac{1}{2}\,(A\,\bar{B} - \bar{A}\,B), \quad H \equiv |B|^2 - \int_0^{|A|^2} Q(\mu, s, K)\,\mathrm{d}s. \tag{38}$$

Note that orbits homoclinic to $(0,0)$ lie in the surface $H = K = 0$. In this case the equation for $a \equiv |A|^2 > 0$ takes the particle-in-potential form

$$\frac{1}{2}\left(\frac{\mathrm{d}a}{\mathrm{d}X}\right)^2 + V(a) = 0, \tag{39}$$

where

$$V(a) \equiv 2\,q_1\,\mu\,a^2 - q_2\,a^3 - \frac{2}{3}\,q_4\,a^4. \tag{40}$$

The shape of the (truncated) potential $V(a)$ depends on the coefficients q_1, q_2 and q_4 determined in the previous section. The essential role played by the coefficient q_4 is now evident.

The behavior of solutions of (39)–(40) when $q_4 < 0$ is shown in Fig. 2. The insets show the effective potential $V(a)$ associated with each region in the (μ, q_2) parameter plane. Shading indicates the existence of homoclinic orbits to $a = 0$; elsewhere, $a = 0$ is a local minimum of the potential and no homoclinic orbits are possible. We see that homoclinic orbits exist in the whole half-space $\mu < 0$, i.e., in the subcritical region. The transition from region (d) to region (c) involves a local bifurcation at $\mu = 0$ which creates a small amplitude homoclinic orbit. The transition from region (a) to region (b) involves a global bifurcation at $\mu = 0$ which creates a large amplitude homoclinic orbit at $\mu = 0$; the turning point of the orbit occurs at $a_0 = -3\,q_2/(2\,q_4) > 0$.

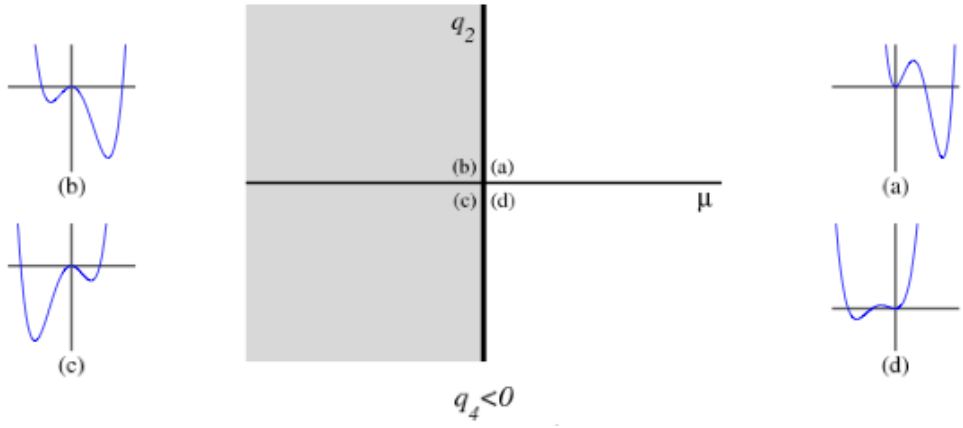

Figure 2: Summary of the behavior of Eqs. (26)–(27) when $q_4 < 0$. Shading indicates the existence of homoclinic orbits to the fixed point at the origin. Insets show $V(a)$ characteristic of the four regions (a)–(d). At $\mu = 0$, there is a local (global) bifurcation in $q_2 < 0$ ($q_2 > 0$). From [9].

The behavior of solutions of Eqs. (39)–(40) when $q_4 > 0$ is summarized in Fig. 3. In this case, homoclinic orbits to $a = 0$ only occur in region (d). In regions (a) and (e), a local minimum of the potential is located at $a = 0$ so a particle that starts at this point remains at rest. In regions (b) and (c), the trajectory of a particle that starts at $a = 0$ is unbounded. The boundary between regions (c) and (d), marked in the figure with a dot-dashed line, is given by

$$\mu^* = -\frac{3\,q_2^2}{16\,q_1\,q_4} \tag{41}$$

and corresponds to the presence of a *heteroclinic cycle* between the origin and the point $a = -3q_2/q_4 > 0$ corresponding to a periodic solution $Z(X)$.

Note that the leading order amplitude equation

$$4\,q_c^2\,Z'' = -\mu\,Z + 4\,q_c^2\,q_2\,Z\,|Z|^2 + \mathcal{O}(\epsilon) \tag{42}$$

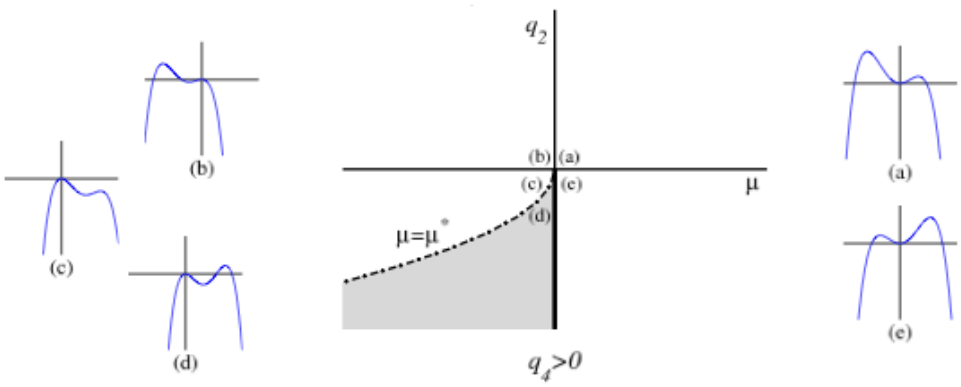

Figure 3: Summary of the behavior of Eqs. (26)–(27) when $q_4 > 0$. Shading indicates the existence of homoclinic orbits to the fixed point at the origin. Insets show $V(a)$ characteristic of the five regions (a)-(e). A heteroclinic cycle is present along the dot-dashed line $\mu = \mu^*$. From [9].

has two types of solutions when $q_2 < 0$, $\mu < 0$. One is constant:

$$Z(X) = \left(\frac{\mu}{4\, q_c^2\, q_2}\right)^{1/2} \mathrm{e}^{i\,\phi} + \mathcal{O}(\epsilon) \tag{43}$$

and corresponds to

$$u(x) = \left(\frac{r}{4\, q_c^2\, q_2}\right)^{1/2} \cos(q_c\, x + \phi) + \mathcal{O}(r), \tag{44}$$

while the other is spatially localized:

$$Z(X) = \left(\frac{\mu}{2\, q_c^2\, q_2}\right)^{1/2} \mathrm{sech}\left(\frac{X\sqrt{-\mu}}{2\, q_c}\right) \mathrm{e}^{i\,\phi} + \mathcal{O}(\epsilon) \tag{45}$$

and corresponds to

$$u(x) = 2\left(\frac{r}{2\, q_c^2\, q_2}\right)^{1/2} \mathrm{sech}\left(\frac{x\sqrt{-r}}{2\, q_c}\right) \cos(q_c\, x + \phi) + \mathcal{O}(r). \tag{46}$$

For the periodic states the spatial phase ϕ is arbitrary; this is not so for the localized states for which the spatial phase ϕ is locked to 0, $\pi/2$, π, $3\pi/2$ when terms beyond all orders are kept. Thus in SH35 four branches of localized states bifurcate from $u = 0$ at $r = 0$. Of these the branches with $\phi = 0, \pi$ correspond to solutions that are reflection-symmetric while those with $\phi = \pi/2, 3\pi/2$ are odd under reflection. The $\phi = 0, \pi$ states are related to one another by the symmetry $u \to -u$ as are the $\phi = \pi/2, 3\pi/2$ states. Thus in a bifurcation diagram that represents the solution amplitude as a function of r one finds two branches, one of even states and the other of odd states. The above calculation shows, in addition, that such localized states are only present when the periodic state bifurcates subcritically and hence are present in the region of coexistence between the periodic state and the trivial state $u = 0$, cf. lecture 6. Analogous results, not discussed here, show that in the case of

SH23 two branches of localized states bifurcate from $u = 0$ at $r = 0$. Both correspond to even states and are characterized by $\phi = 0, \pi$. In this case the $\phi = 0, \pi$ states are no longer related by symmetry and the bifurcation diagram therefore also consists of two distinct branches.

The selection of the spatial phase ϕ is a highly subtle point [7, 8, 10]; however, one can get a good appreciation of the issues involved by substituting the approximate solution (46) into Eq. (1). Note in particular that states of the form (46) have no particular symmetry unless ϕ takes one of the special values just mentioned. Such asymmetric states are in fact present but are only created in *secondary* bifurcations from the primary branches of localized states that bifurcate from $u = 0$. Figure 4 shows schematically the number and connectivity of the resulting localized states in the SH23 and SH35 cases: in the SH35 case four asymmetric branches are created at finite amplitude and connect each of the two even branches with each of the two odd branches (see Sect. 7 below).

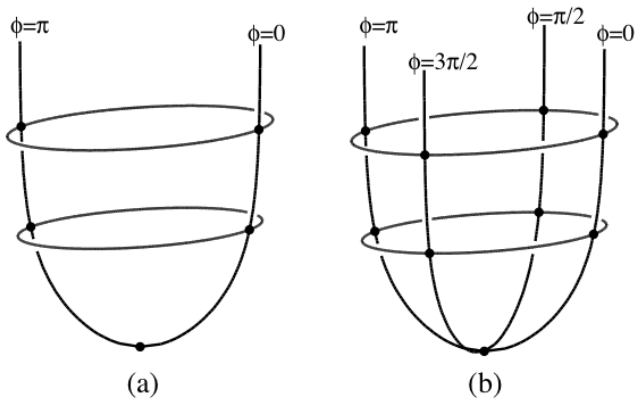

Figure 4: Schematic diagram showing the number and connectivity of the branches of localized states for (a) SH23 and (b) SH35. In (a) each rung consists of two distinct branches connecting the two constant phase branches; in (b) each rung consists of four distinct branches connecting each constant phase branch with its two neighbors. From [3].

6 Example: Natural doubly diffusive convection

Natural convection is a term given to convection driven by horizontal temperature convection. When the fluid is a mixture of two components (eg., water and salt) and the gradients of both temperature and (salt) concentration are horizontal we speak of natural doubly diffusive convection.

Motivated by the results in Sect 2.5.1 of lecture 6, we examine an infinite vertical slot filled with such a mixture. We adopt no-slip boundary conditions on the vertical plates and suppose that these are maintained at fixed but different temperatures and concentrations. These can be arranged such that the buoyancy force due to the temperature field is exactly balanced by the buoyancy force arising from the concentration field. In this case the system possesses a conduction state characterized by linear variation of temperature and

concentration across the system and no flow. This state will be stable for small temperature differences but is expected to lose stability as this temperature difference, traditionally measured by the dimensionless Grashof number $Gr \equiv g\alpha\Delta T\ell^3/\nu^2$, increases. Here α is the coefficient of thermal expansion, ΔT is the imposed temperature difference, and ℓ is the separation between the two plates, assumed to be placed at $x = 0, \ell$.

Linear analysis about the conduction state with respect to two-dimensional spatially growing perturbations looks for solutions of the time-independent linearized equations of the form $(\tilde{u}, \tilde{w}, \tilde{T}, \tilde{C})(x) \exp(\lambda z)$, where $\lambda \equiv q_r + i\, q_i$ is the spatial growth rate. This formulation leads to the dimensionless equations [2]:

$$\lambda\,\tilde{u} = -\partial_x\tilde{p} + \nabla^2\tilde{u} \tag{47}$$

$$\lambda\,\tilde{w} = -\partial_z\tilde{p} + \nabla^2\tilde{w} + Gr\,(\tilde{T} - \tilde{C}) \tag{48}$$

$$0 = \partial_x\tilde{u} + \partial_z\tilde{w} \tag{49}$$

$$\lambda\,\tilde{T} = \tilde{u} + \frac{1}{Pr}\,\nabla^2\tilde{T} \tag{50}$$

$$\lambda\,\tilde{C} = \tilde{u} + \frac{1}{Sc}\,\nabla^2\tilde{C} \tag{51}$$

with the boundary conditions $\tilde{u} = \tilde{w} = \tilde{T} = \tilde{C} = 0$ at $x = 0, 1$. Here $Pr \equiv \nu/\kappa$ is the Prandtl number and $Sc \equiv \nu/D$ is the Schmidt number. In contrast to the Swift-Hohenberg equation, this problem is an eigenvalue problem for λ that has to be solved for each value of Gr and fixed values of the remaining parameters. Such a problem has in general an infinite number of eigenvalues, but we are interested here only in the leading eigenvalues, i.e., the eigenvalues whose real parts are closest to zero.

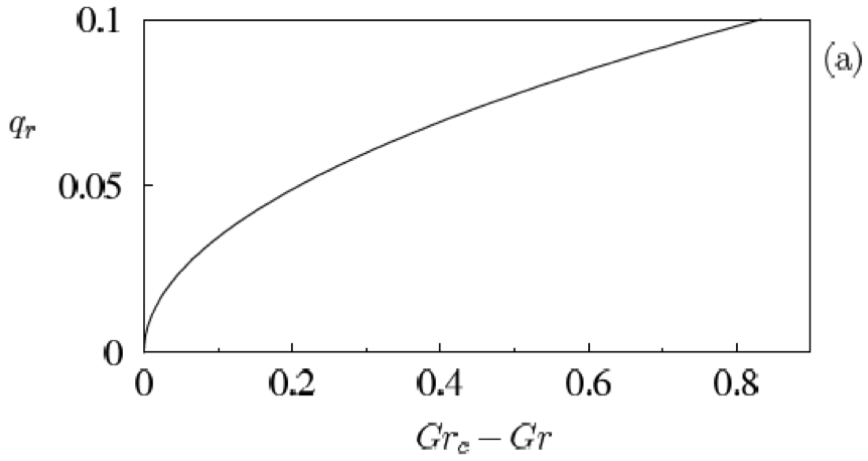

Figure 5: The spatial growth rate q_r as a function of the distance from the critical Grashof number Gr_c in the subcritical regime $Gr < Gr_c$. From [2].

Solution of this problem indicates that the four leading eigenvalues form a pair of purely imaginary eigenvalues $q_r = 0$, $q_i \equiv q_c = \pm 2.5318$ of double multiplicity when $Gr_c = 650.9034$. Thus at this value of Gr the solution takes the form of a spatially periodic wavetrain. Moreover, one also finds that (Fig. 5)

- $Gr < Gr_c$: $\lambda = \pm i\, q_c \pm O(\sqrt{Gr_c - Gr})$
- $Gr > Gr_c$: $\lambda = \pm i\, q_c \pm i\, O(\sqrt{Gr - Gr_c})$,

implying that the leading spatial eigenvalues behave exactly as in the Swift-Hohenberg equation. This is a consequence of the reversibility of the equations with respect to the symmetry Δ: $(x, z) \to (1 - x, -z)$, $(\tilde{u}, \tilde{w}, \tilde{T}, \tilde{C}) \to -(\tilde{u}, \tilde{w}, \tilde{T}, \tilde{C})$ which plays exactly the same role as the symmetry $x \to -x$, $u \to u$ in SH23. Thus in this case we expect *two* branches of localized states of even parity (with respect to Δ), corresponding to $\phi = 0, \pi$. Theory predicts that these branches will only be present if the coefficient q_2 in the normal form (26)–(29) is negative. This will be so if the branch of periodic states with wavenumber q_c bifurcates *subcritically*. The theory also predicts that if this is the case the branches of localized states also bifurcate subcritically. Thus the prediction of localized states in the present system reduces to the computation of the direction of branching of periodic states. This is a standard calculation that can be done in a periodic domain of period $2\pi/q_c$, i.e., in a small domain, although it may have to be done numerically. For $Pr = 1$, $Sc = 11$ this bifurcation is indeed subcritical [2]; moreover, two branches of even parity localized states are present and these also bifurcate subcritically, exactly as predicted by SH23 [4].

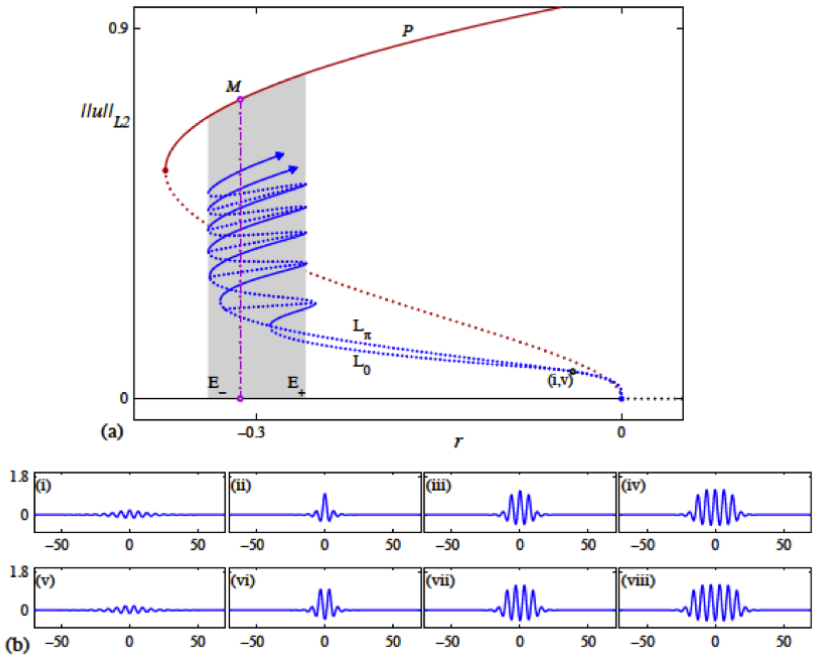

Figure 6: (a) Bifurcation diagram showing the snakes-and-ladders structure of localized states. Away from the origin the snaking branches L_0 and L_π are contained within a snaking region (shaded) between E_- and E_+, where $r(E_-) \approx -0.3390$ and $r(E_+) \approx -0.2593$. Solid (dotted) lines indicate stable (unstable) states. (b) Sample localized profiles $u(x)$: (i)–(iv) lie on L_0, near onset and at the 1st, 3rd, and 5th saddle-nodes from the bottom, respectively; (v)–(viii) lie on L_π, near onset and at the 1st, 3rd, and 5th saddle-nodes, respectively. Parameters: $b_2 = 1.8$. From [4].

7 Snakes-and-ladders structure of the pinning region: SH23

In this section we describe what happens when the small amplitude results are extended into the fully nonlinear regime using numerical continuation. We describe the results for SH23,

$$u_t = r\,u - (q_c^2 + \partial_x^2)^2\,u + b_2\,u^2 - u^3. \tag{52}$$

Figure 6 shows the L_2 norm, $||u|| \equiv \int_{-\infty}^{\infty} u^2(x)\,\mathrm{d}x$, of the localized states $L_{0,\pi}$ as a function of the bifurcation parameter r. The L_2 norm (per unit length) of the periodic state, labeled P, is shown for comparison. The figure shows that the two branches of even parity localized states that bifurcate subcritically from $u = 0$ at $r = 0$ enter a shaded region, hereafter the *snaking* or *pinning* region, in which they undergo repeated saddle-node bifurcations as they snake across the region. These saddle-nodes converge exponentially rapidly to a pair of r-values, hereafter $r(E_-)$ and $r(E_+)$, representing the boundaries of the shaded region. The convergence is monotonic and from the right in both cases. The lower panels show a series of profiles of $u(x)$ at successive saddle-nodes and reveal that the states labeled L_0 are characterized by a peak in the center while those labeled L_π have a dip in the center. The panels show that each localized state nucleates a pair of peaks or cells, one on either side, in the vicinity of $r = r(E_-)$. As one proceeds up the branch to the next fold on the right, at $r = r(E_+)$, the peaks or cells grow to the height of the coexisting periodic state P and the branch turns around to repeat the process. Thus as one proceeds up the intertwined $L_{0,\pi}$ branches the localized states repeatedly add cells on either side while preserving their parity, each back-and-forth oscillation increasing the width of the state by two wavelengths $2\pi/q_c$. On the real line this process continues indefinitely as both branches approach the periodic state P.

Figure 7(a) is a close-up view of Fig. 6, focusing on the rung states which connect the $L_{0,\pi}$ snaking branches. These states are asymmetric with respect to the reflection $x \to -x$ (Fig. 7(b)). In generic translation-invariant systems such states would drift. This is not so here because of the gradient structure of Eq. (52) and the rung states correspond to stationary states. The rungs are created in pitchfork bifurcations which break the $u(x) \to u(-x)$ symmetry of the $L_{0,\pi}$ states. Consequently each rung in the figure corresponds to two states related by reflection symmetry and hence of identical L_2 norm.

The location of these pitchfork bifurcations is determined by linearizing Eq. (52) about a localized solution $u = u_0(x)$ and solving the eigenvalue problem

$$\mathcal{L}[u_0(x)]\,\tilde{U} \equiv \{r - (q_c^2 + d_x^2)^2 + 2b_2\,u_0 - 3u_0^2\}\tilde{U} = \sigma\tilde{U} \tag{53}$$

for the eigenvalues σ and for the corresponding eigenfunctions $\tilde{U}$. This problem has to be solved numerically; if the domain used is much larger than the length of the localized structure the resulting eigenvalues will be independent of the boundary conditions imposed at the boundary. The eigenvalues comprise the spectrum of the linear operator $\mathcal{L}[u_0(x)]$ and this spectrum consists of two components depending on the symmetry of the eigenfunctions. Even eigenfunctions share the symmetry of $u_0(x)$ and correspond to *amplitude* modes. These modes are neutrally stable ($\sigma = 0$) at saddle-node bifurcations. Odd eigenfunctions will be called phase modes. There is always one neutrally stable phase mode, the Goldstone mode. To see this we consider two stationary solutions of Eq. (52), $u_0(x+d)$ and $u_0(x)$, i.e., a pair

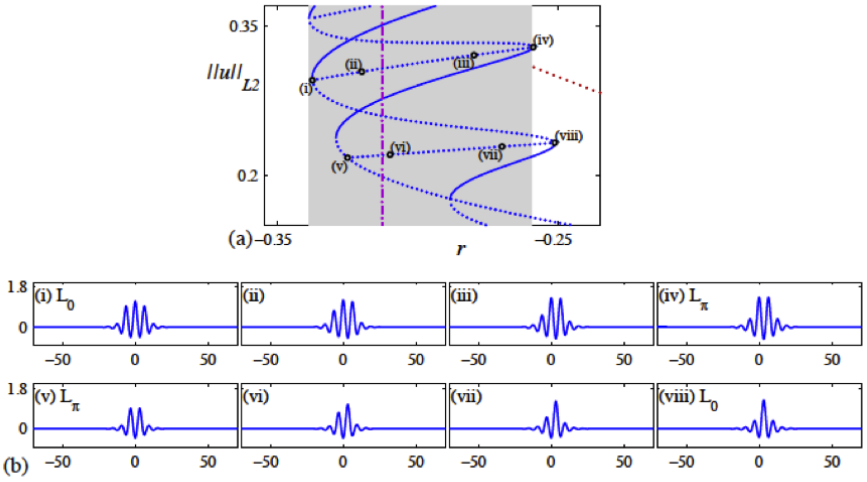

Figure 7: (a) Close-up view of Fig. 6(a) showing two rungs connecting the snaking branches L_0 and L_π. Solid (dotted) lines indicate stable (unstable) states. (b) The profiles (i) and (viii) lie on L_0 while (iv) and (v) lie on L_π. The remaining profiles are asymmetric and lie on the rungs. From [4].

of solutions related by translation. We subtract the equations satisfied by these solutions, divide by d and take the limit $d \to 0$. The result is

$$\mathcal{L}[u_0(x)]\, u_0' = 0, \tag{54}$$

implying that u_0' is a neutrally stable eigenfunction of $\mathcal{L}[u_0(x)]$ for all parameter values. Evidently the presence of this mode is a consequence of the translation invariance of the system. In addition, there is a discrete set of neutrally stable phase modes associated with symmetry-breaking bifurcations of $u_0(x)$, i.e., the creation of the rung states. Figure 8(b) shows each of these eigenfunctions, computed as described above, for a relatively long localized state high up the snakes-and-ladders structure. We make two important observations: the amplitude and phase modes are localized in the vicinity of the fronts bounding $u_0(x)$; by adding and subtracting these modes we construct eigenfunctions localized at one or other front. This observation implies that both the saddle-nodes and the pitchfork bifurcations are associated with instabilities of individual fronts. This picture becomes better and better as the length of $u_0(x)$ becomes longer, i.e., for long localized structures the fronts at either end can be treated independently, and in this regime the localized structure $u_0(x)$ can be considered to be a bound state of a pair of fronts.

Figure 9 shows the eigenvalues σ along the $L_{0,\pi}$ snaking branches starting from the primary bifurcation at $r = 0$ and moving upward along each branch. The phase and amplitude modes are labeled. We see that close to $r = 0$ both states are amplitude-unstable, as expected of a subcritical bifurcation. In contrast, the phase eigenvalues are almost zero, with L_0 phase-stable and L_π phase-unstable. Each zero of the amplitude eigenvalue generates a saddle-node bifurcation and since σ oscillates about zero each solution

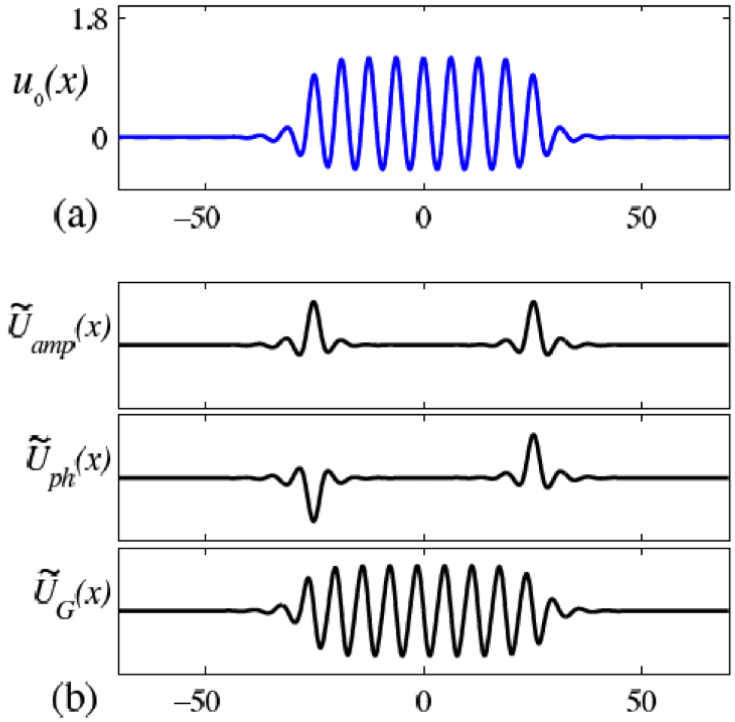

Figure 8: (a) A localized state $u_0(x)$ at E_- high up the L_0 snaking branch. (b) From top to bottom, the corresponding amplitude, phase, and translational modes. Parameters: $b_2 = 1.8$, $r = -0.3390$. From [4].

gains and loses amplitude stability at successive saddle-nodes. The phase eigenvalue also oscillates about zero and tracks ever more closely the amplitude eigenvalue. Thus as one proceeds up the snaking structure the bifurcations to the rung states approach ever closer to the saddle-nodes (in fact exponentially rapidly), although they always remain on the unstable part of the branch. Thus near a saddle-node of a long localized structures one finds three near-marginal modes, the amplitude and phase modes, as well as the Goldstone mode. This fact will be useful in interpreting the dynamical behavior one finds just outside of the snaking region as discussed in lecture 8.

The above results account for the stability changes indicated in Figs. 6 and 7; no other eigenvalues are ever involved. A similar calculation shows that the asymmetric rung states are always unstable. Altogether, the results show that in the snaking region one finds an *infinite* number of coexisting stable symmetric localized structures of different lengths. These come in two types, with maxima or minima in their symmetry plane. Each state can be realized in the time-dependent problem by selecting an appropriate finite amplitude (localized) initial condition. The results for SH35 are essentially identical.

7.1 Multipulse states

In fact things are much more complicated. This is because the snaking region also contains a variety of multipulse states [6]. The term multipulse refers to the fact that the phase space

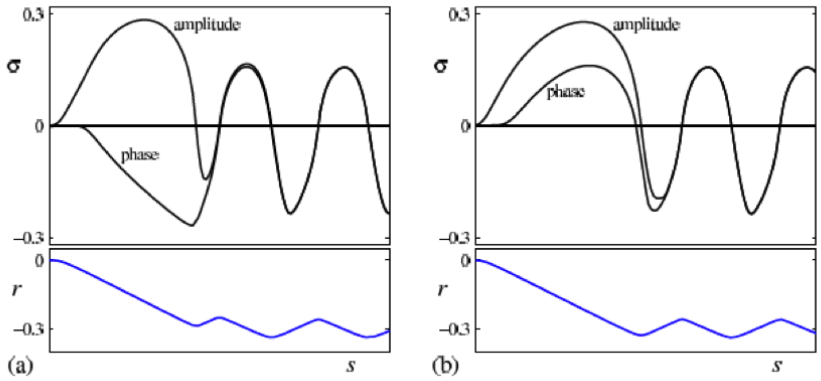

Figure 9: Spectrum of growth rates σ along the (a) L_0 and (b) L_π branches of localized states in SH23 as a function of the arc length s along each branch, measured from the bifurcation at the origin. The lower panels show the location in r of the corresponding branches. Parameters: $b_2 = 1.8$. From [4].

trajectory comes close to the origin after the first localized state (pulse) but only forms a homoclinic orbit to the origin after a second (two-pulse) or more (multipulse) excursions. Multipulse states should be thought of as (weakly) bound states of two or more localized structures of the type we have been discussing.

Multipulse states can be equispaced forming a periodic array of identical localized structures. Such states are not very different from the single pulse states and it will come as no surprise that they also snake (Fig. 10). But one can also find two-pulse states consisting of identical pulses that are separated by a distance that is less than the average interpulse spacing. The locations of such pulses are 'quantized' in terms of half wavelengths π/q_c. Specifically, two identical L_0 pulses can have a local maximum or a local minimum at the half way location between them [6]. On a periodic domain of a large but finite period there is thus a finite number of such these states. These do not snake but instead lie on nested isolas. The nested isolas in turn form a vertical stack of like states, each stack consisting of bound states of localized states of ever increasing length (Fig. 11). The break-up of the two-pulse states into isolas as soon as they are not evenly spaced is a consequence of asymmetry in the interaction between the pulses.

In addition, one can also find two-pulse states consisting of different localized states [6]. Thus the snaking region consists of an unimaginable variety of different localized structures a large fraction of which can be stable.

7.2 Finite size effects

Figure 10(a) reveals two additional insights. The figure is computed on a periodic domain of length Γ with periodic boundary conditions. We see that for $\Gamma < \infty$ the multiple bifurcation at $r = 0$ breaks up into a primary bifurcation to a periodic wavetrain, together with a secondary bifurcation from this state to the (two) branches of localized states that takes

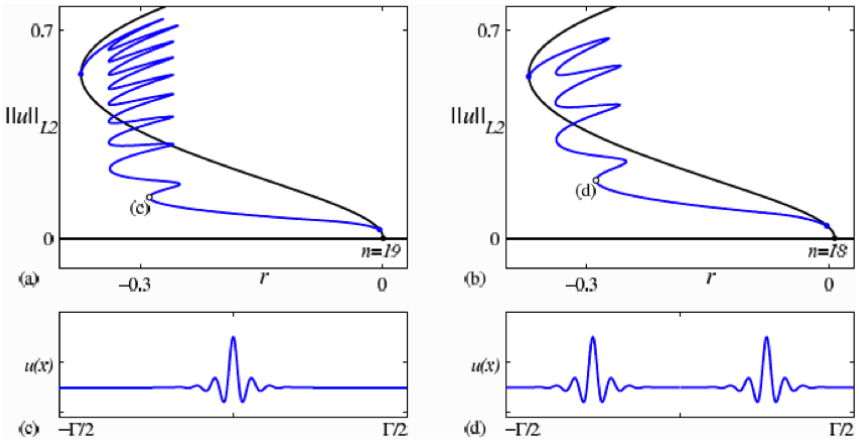

Figure 10: Bifurcation diagrams showing (a) a L_0 single-pulse snaking branch, and (b) a two-pulse snaking branch consisting of two evenly spaced copies of L_0, both on the same periodic domain of period Γ. (c,d) Sample profiles at the points indicated in the bifurcation diagrams; the states in (d) are separated by $\Gamma/2$. Similar branches consisting of L_π pulses are omitted. Parameters: $b_2 = 1.8$, $\Gamma = 118$. From [6].

place at small but nonzero amplitude. This is almost certainly the reason why spatially localized states have been discovered only recently: almost all textbooks on hydrodynamic instability immediately impose periodic boundary conditions when studying the instability of a homogeneous base state. This inocuous assumption pushes the bifurcation to localized states to finite amplitude where its discovery requires not only knowledge of the finite amplitude periodic state but also a linear stability analysis of a nontrivial periodic state requiring Floquet theory. As we have seen the problem becomes so much easier if posed on the whole real line!

Figure 10(a) also reveals that on a finite periodic domain snaking does not continue for ever. Once the localized structure has grown to fill the domain no additional growth is possible and the branch of localized states exits the snaking region and terminates near the fold on the branch of periodic states. The details of this transition are in general complex since they depend on exactly how much space is left, i.e., on Γ mod λ_c, where λ_c is the critical wavelength [1]. Observe, however, that near the fold the localized states resemble holes in an otherwise periodic wavetrain. We shall come across hole states in subsequent lectures. For now the lesson learnt is that holes are related to secondary bifurcations near the fold of the periodic state.

Note, finally, that Fig. 10(b) shows that on a smaller domain, here $\Gamma/2$, a single pulse state bifurcates from the periodic states at a larger amplitude, and that the resulting branch also terminates further from the fold.

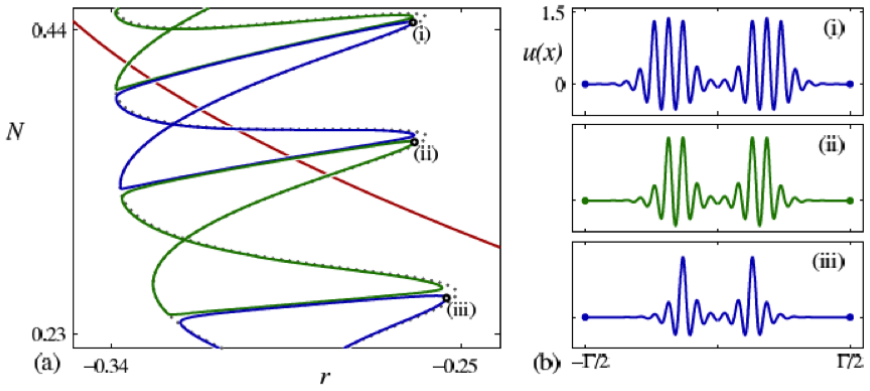

Figure 11: (a) Bifurcation diagram showing isolas of symmetric but unevenly spaced two-pulse states. In the main diagram, only one isola at each level of the isola stack is plotted to avoid clutter. (b) Profiles at the points labeled in the bifurcation diagram; the states are separated by distances less than $\Gamma/2$. Parameters: $b_2 = 1.8$, $\Gamma = 118$. From [6].

References

[1] A. Bergeon, J. Burke, E. Knobloch and I. Mercader. Eckhaus instability and homoclinic snaking. *Phys. Rev. E 78*, 046201, 2008.

[2] A. Bergeon and E. Knobloch. Spatially localized states in natural doubly diffusive convection. *Phys. Fluids* **20**, 034102, 2008.

[3] J. R. Burke. Localized States in Driven Dissipative Systems, PhD Thesis, University of California at Berkeley, 2008.

[4] J. Burke and E. Knobloch. Localized states in the generalized Swift-Hohenberg equation. *Phys. Rev. E* **73**, 056211, 2006.

[5] J. Burke and E. Knobloch. Homoclinic snaking: Structure and stability. *Chaos* **17**, 037102, 2007.

[6] J. Burke and E. Knobloch. Multipulse states in the Swift-Hohenberg equation. *Discrete and Continuous Dyn. Syst. Suppl.*, pp. 109–117, 2009.

[7] S. J. Chapman and G. Kozyreff. Exponential asymptotics of localized patterns and snaking bifurcation diagrams. *Physica D* **238**, pp. 319–354, 2009.

[8] A. D. Dean, P. C. Matthews, S. M. Cox and J. R. King. Exponential asymptotics of homoclinic snaking. *Nonlinearity* **24**, pp. 3323–3352, 2011.

[9] G. Iooss and M. C. Pérouème. Perturbed homoclinic solutions in reversible 1:1 resonance vector fields. *J. Diff. Eq.* **102**, pp. 62–88, 1993.

[10] G. Kozyreff and S. J. Chapman. Asymptotics of large bound states of localized structures. *Phys. Rev. Lett.* **97**, 044502, 2006.

[11] L. Yu. Glebsky and L. M. Lerman. On small stationary localized solutions for the generalized 1-D Swift–Hohenberg equation. *Chaos* **5**, pp. 424–431, 1995.